JOURNAL OF MATERIALS SCIENCE 25 (1990) 4667–4677

Microstructural and kinetic aspects of devitrification of $Fe_{40}Ni_{40}B_{20}$ metallic glass

V. S. RAJA*, KISHORE, S. RANGANATHAN
Department of Metallurgy, Indian Institute of Science, Bangalore 560 012, India

The crystallization characteristics of Vitrovac 0040 commercial glass with a composition of $Fe_{40}Ni_{40}B_{20}$ have been investigated in detail using differential scanning calorimetry, X-ray diffraction, optical and electron microscopy techniques. The results confirm the simultaneous occurrence of four kinds of crystalline precipitates with differing growth behaviour. The overall transformation kinetics of the eutectic product which had the highest growth rate has been documented. The result yielded a low value of 2.08 for the Avrami exponent, which has been attributed to its athermal nucleation and anisotropic growth behaviour. The diffusivity obtained from interlamellar spacings has been found to agree well with the previous values obtained by direct measurement using secondary ion mass spectroscopy for boron diffusion.

1. Introduction

Fe–Ni base metallic glasses are among the widely investigated alloy systems. In this, $Fe_{40}Ni_{40}B_{20}$ is a simple ternary system whose thermal behaviour has been investigated by both direct and indirect methods [1–15]. Scott and Kursumovic [1] and Van den Beukel *et al.* [2, 3] have studied the relaxation behaviour of the glass below glass transition temperature. In a noteworthy study, employing atom probe field-ion microscopy, Piller and Haasen [4] provided evidence for phase separation.

In his pioneering study, Luborsky [5] reported the crystallization temperature, $T_x = 715\,K$, and an apparent activation energy, $E_c = 280\,kJ\,mol^{-1}$, using differential scanning calorimetry (DSC) and magnetic coercivity measurements. Stubicar *et al.* [6] characterized the isochronal crystallization using X-ray diffraction (XRD). They claimed that an orthorhombic $(FeNi)_3B$ crystallized first from an amorphous matrix around 673 K and was followed by the appearance of γ-FeNi above 873 K. The boride phase later transformed to ν-FeNi above 1073 K. In a study, again using XRD, Steffen and Liedtke [7] reported the reverse order. γ-FeNi appeared first and was followed by $(FeNi)_3B$.

The real complexity of the reactions has been brought out by the use of transmission electron microscopy (TEM). These studies were parallel to the present investigation, a preliminary report of which has been presented elsewhere [8]. Muller and Heimendahl [9] observed that three types of crystals nucleated simultaneously and grew at varying rates. They identified the three types as (1) a eutectic mixture of γ-FeNi and orthorhombic $(FeNi)_3B$, (2) a eutectic mixture of γ-FeNi and fcc $(FeNi)_{23}B_6$ and (3) a solid solution of γ-FeNi. The first eutectic mixture displayed the highest growth rate. However, Duhaj and Svec [10] found that an fcc solid solution crystallized first and then transformed into a eutectic mixture of γ-FeNi and a tetragonal $(FeNi)_3B$ boride. A second eutectic reaction started a little later and gave rise to an fcc solid solution and an orthorhombic $(FeNi)_3B$. They claimed that $(FeNi)_{23}B_6$ observed by Muller and Heimendahl was, in fact, only the tetragonal boride. In a recent investigation, Cermak *et al.* [11] have noted the influence of argon and hydrogen during isochronal annealing of the glass.

Incidental to their atom probe field-ion microscopic study, Pillar and Haasen [4] have reported a two-stage reaction in their DSC experiments and interpreted it as due to a primary crystallization into γ-FeNi followed by a eutectic crystallization into γ-FeNi and $(FeNi)_3B$. They deduced the activation energies via Kissinger plots to be 335 and 370 kJ mol^{-1}, respectively.

A related but classical investigation of $Fe_{40}Ni_{40}B_{20}$ glass is a *tour de force* by Cahn *et al.* [12]. Using secondary ion mass spectroscopy they determined self-diffusion of boron to be between 2×10^{-9} and $7 \times 10^{-18}\,m^2\,sec^{-1}$ in the range 613 and 643 K.

The effect of processing parameter on the thermal stability of $Fe_{40}Ni_{40}B_{20}$ has been the subject of study by a few investigators. Chi *et al.* [13] reported very little, if any, influence of quenching rate on the thermal stability of the glass as they obtained the same activation energies irrespective of quenching rates. The activation energies deduced by them (444 kJ mol^{-1}) are, however, significantly higher than those reported by Luborsky [5]. Takayama and Oi [14], while noticing no variation in crystallization temperatures, reported a higher stability for those alloys obtained by a slow cooling rate. According to Koster *et al.* [15], a high contact time with the copper wheel necessary for the

Present address: Corrosion Science and Engineering, Department of Metallurgical Engineering, Indian Institute of Technology, Powai, Bombay 400 076, India.

0022–2461/90 $03.00 + .12

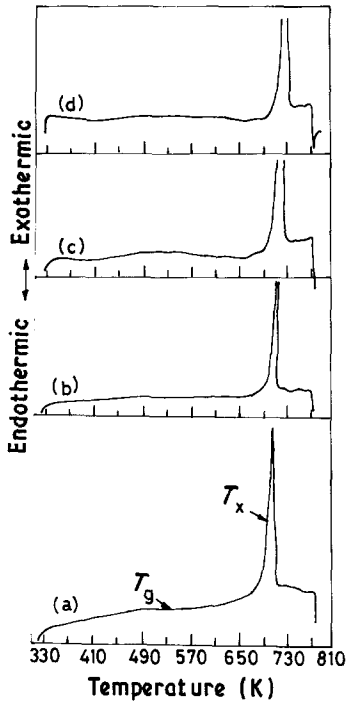

Figure 1 Differential scanning calorimetry curves showing the variation of T_p and T_g with heating rate: (a) 5 K min^{-1}, (b) 10 K min^{-1}, (c) 20 K min^{-1} and (d) 40 K min^{-1}.

higher cooling rate, inherently induced a greater number of nucleation sites on the surface, thereby promoting heterogeneous nucleation at the contact surface.

In spite of the number of studies undertaken, the following questions remain to be answered: (1) the number of stages in the reaction (one or two); (2) the nature of the reaction (primary, polymorphic or eutectic); (3) transformation products: while the investigators are agreed on the occurrence of orthorhombic $(FeNi)_3B$, there is considerable disagreement about the production of tetragonal $(FeNi)_3B$ and fcc $(FeNi)_{23}B_6$; (4) possible phase separation.

2. Experimental procedure

The metallic glass Vitrovac 0040 supplied by Vacuumschmelze, West Germany, was in the form of 20 mm × 0.04 mm ribbon having a nominal composition of $Fe_{40}Ni_{40}B_{20}$. The samples were tested for their amorphous nature by X-ray and electron microscopy. The

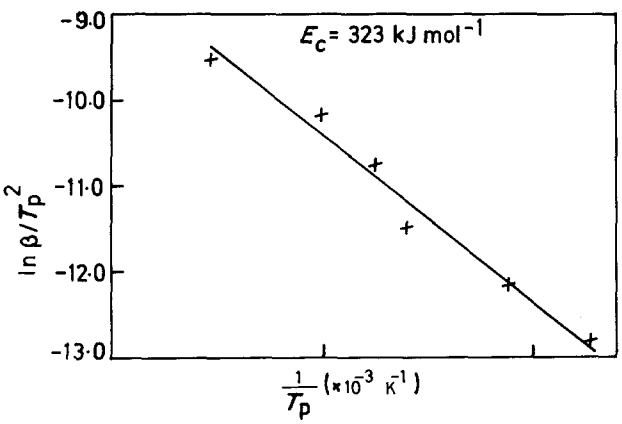

Figure 2 Kissinger plot of Vitrovac 0040.

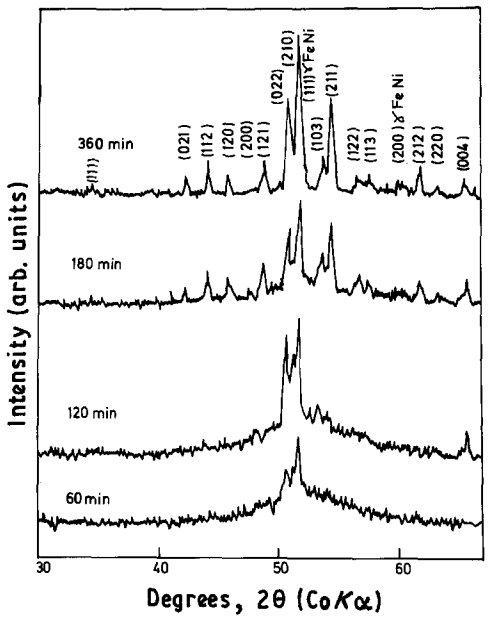

Figure 3 X-ray diffractograms showing the progress of crystallization of Vitrovac 0040 glass for the isothermal annealing at 653 K. The $(h\,k\,l)$ planes belong to θ-(FeNi)B. Reflections of γ-(FeNi) are identified in the figure.

details of the experimental procedure followed in carrying out DSC analysis can be found elsewhere [16]. Isothermal heat treatments were carried out below T_x in the temperature range 643 to 673 K in a low-temperature salt-bath furnace. The temperature of the salt bath was controlled to an accuracy of ±1 K. After heat treatment, the samples were quenched in water.

The annealed samples were mounted on a Perspex disc using Araldite adhesive. Subsequent to this, the samples were polished by conventional metallographic techniques, etched with acid $FeCl_3$ and observed in a Neophot 21 optical microscope. The volume fraction transformed was determined using the standard point count technique [17]. About three thousand points were counted to ensure fairly reliable results. For transmission electron microscopy, square specimens of 3 mm dimensions were cut and electrolytically polished in a mixture 90% acetic acid and 10% perchloric acid maintained at 10° C and using a twin jet Tenupol polisher with an applied 25 d.c. V. The specimens were viewed under Phillips EM 301 microscope operating at 100 kV. X-ray diffraction studies were conducted with a Phillips 1140 X-ray diffractometer. The annealed samples were directly mounted on the holder and Co$K\alpha$ radiation of wavelength 0.179 01 nm was used for the studies.

3. Results

3.1. Differential scanning calorimetry

The glass was subjected to non-isothermal heating rates of 1.25, 2.5, 5, 10, 20 and 40 K min^{-1}. The shift in peak temperature, T_p, with heating rate is illustrated in Fig. 1 for the rates 5, 10, 20 and 40 K min^{-1}. The variation of T_p with heating rate has been used to compute the activation energy for crystallization (Fig. 2) using the Kissinger relation [18].

$$\ln (\beta/T_p^2) = -(E_c/RT_p) + C$$

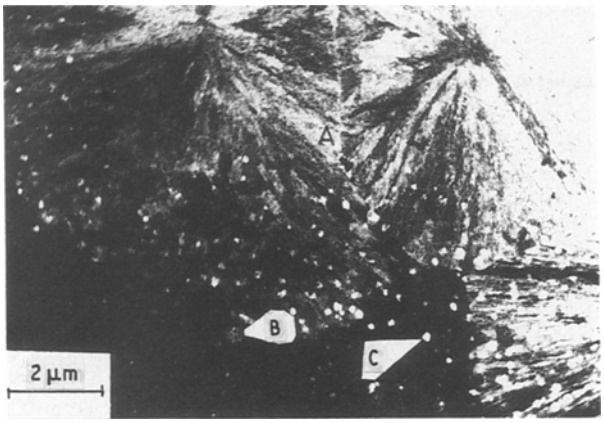

Figure 4 Low-magnification transmission electron micrograph of the partially crystallized glass: (A) γ-FeNi + θ-$(FeNi)_3B$, (B) γ-FeNi + fcc $(FeNi)_{23}B_6$ and (C) γ-FeNi crystals.

where β, T_p, E_c and C are the heating rate, peak temperature, apparent activation energy and a constant. The activation energy was found to be 323 kJ mol^{-1}.

3.2. X-ray diffraction

The as-received glass showed a broad peak around a glancing angle of 2θ equalling 53° corresponding to k $(= 4\pi \sin \theta/\lambda) = 31.3\,\text{nm}^{-1}$, confirming the amorphous nature of the alloy. The glass annealed between 643 and 673 K for various time intervals showed peaks corresponding to γ-FeNi and orthorhombic $(FeNi)_3B$ in the X-ray diffraction. The progressive formation of the two phases with time for an annealing temperature of 653 K is shown in Fig. 3. The lattice parameters were deduced from the d-values. The lattice parameters of the orthorhombic $(FeNi)_3B$ phase correspond to $a = 0.443$, $b = 0.537$ and $c = 664$ nm and the lattice constant of the γ-FeNi is 0.357 nm, which are close to those observed earlier [7].

3.3. Microstructural observations

The bulk samples isothermally aged at 643, 653, 663 and 673 K were examined under TEM after electropolishing them. The annealed glass disclosed three different kinds of crystals nucleating simultaneously and growing at different rates, further confirming the single exothermic peak observed in the DSC. The microstructure of a partly crystallized glass (annealed 663 K, 1 h) illustrating the three kinds of crystals, marked A, B and C, is shown in the TEM bright-field image (Fig. 4). In different regions of the foils the crystals grow in random orientation. In general, no morphological or structural variations can be noticed within the four isothermal temperatures (643 to 673 K) of investigation. The phase marked A has grown fastest and has a typical eutectic morphology. This eutectic nature is clearly seen in the fully crystallized condition in Fig. 5. The micrograph indicates that the four eutectic crystals are random in orientation. As a result, the fine eutectic structure in them has a varying appearance of rods and dot-like (salt and pepper) forms.

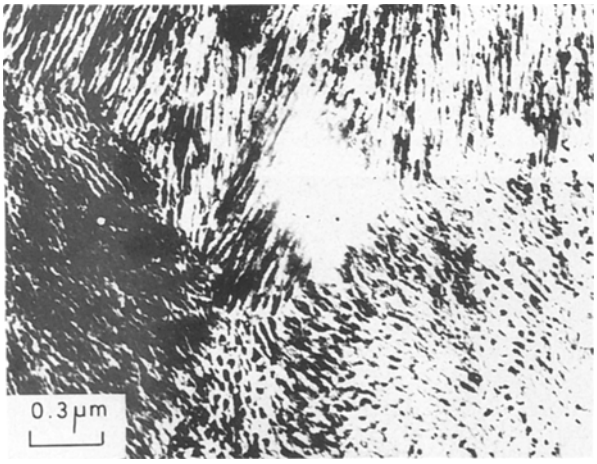

Figure 5 The two-phase eutectic structure of A-type crystals in the fully crystallized glass.

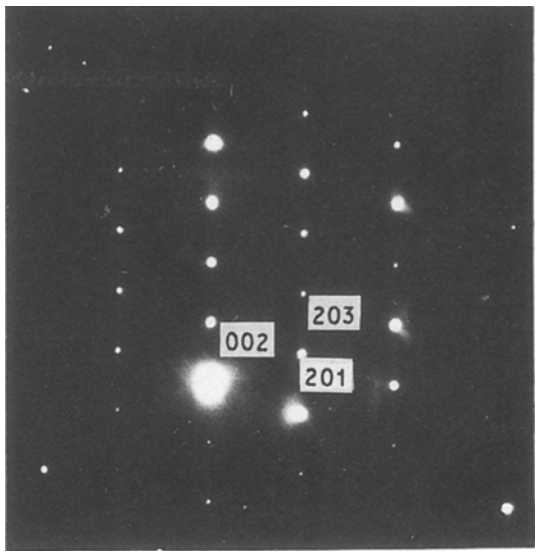

Figure 6 SAD pattern of A-type crystals taken along two different zone axes. The patterns are indexed for θ-$(FeNi)_3B$ phase.

Selected-area diffraction (SAD) patterns were obtained on the A-type crystal. Fig. 6 shows a typical pattern obtained on this crystal that can be indexed satisfactorily for orthorhombic $(FeNi)_3B$ boride phase. Although the pattern is simple, having clear spots, some of the SAD patterns were found to be complex consisting of multiple spots, and streaking may be due to either twins or a microcrystalline nature.

The lattice parameters obtained from SAD patterns are in agreement with the values obtained from the X-ray diffraction measurements within the allowable experimental error.

The eutectic crystals revealed a regular growth in the present study in contrast to the irregular morphology reported earlier [9]. A comparison of various cross-sections of the crystals indicates a rod-like growth of the crystals with an aspect ratio of 4.0. The micrograph of a transverse section of a crystal is shown in Fig. 7. The sides of the crystals are somewhat flattened. The bright-field image shows four contrasting regions, as reported in the case of $Fe_{40}Ni_{40}P_{14}B_6$ [19] and the internal structure at high magnification revealed platelets of eutectic phases in the bright regions and spheroid-like structure in the dark

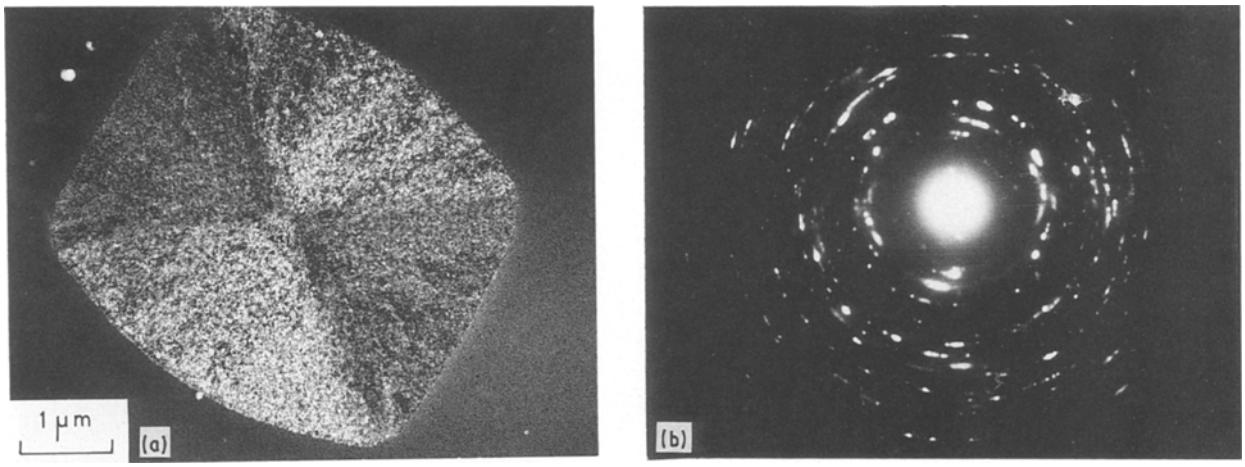

Figure 7 (a) The bright-field image of a transverse section of the A-type crystal and (b) the corresponding electron diffraction pattern.

regions. The electron diffraction pattern taken by covering all four regions demonstrates multiple orientations of the two phases within the crystal (Fig. 7) as is evident from the complex spotted-ring pattern.

The longitudinal section of the eutectic crystal, having an aspect ratio ≈ 4, is shown in Fig. 8. The TEM image also shows a transverse section of the crystal which has a circular cross-sectional image shown in the same figure. The above two observations unambiguously demonstrate the anisotropic growth behaviour of the crystals. The SAD pattern from the longitudinal section of the crystal is shown in Fig. 8. The bright-field image is rotated in the clockwise direction through 39° with respect to the SAD pattern to correct the rotation of the image. It is seen that the major axis of the crystal lies along [1 0 0] of the orthorhombic phase and the streaking in the SAD pattern may correspond to either faulted structure or the fineness of the rods. From the SAD pattern shown in the above figure it can easily be noticed that the streaking direction is along [0 1 1]. In addition to streaking, the above patterns also have extra spots which could mainly arise from the twins present in the orthorhombic phase. For every main spot of the pattern two extra spots are seen. The high magnification image (Fig. 9) clearly indicates twins in the orthorhombic phase. It should be remarked that these twins lie not only normal to the growth direction of the eutectic rods but also inclined to their growth direction.

Microstructural details and an SAD pattern of yet another kind of eutectic crystal labelled "B" are shown in Fig. 10. The B-type eutectic crystals consist of platelets and spheroids of γ-FeNi in $(FeNi)_{23}B_6$ phase as delineated in the transmission electron micrograph (Fig. 10). The electron diffraction pattern can be indexed on the basis of f c c $(FeNi)_{23}B_6$. It should be remarked that contrary to γ-FeNi + orthorhombic $(FeNi)_3B$ crystals, the present one produces clear

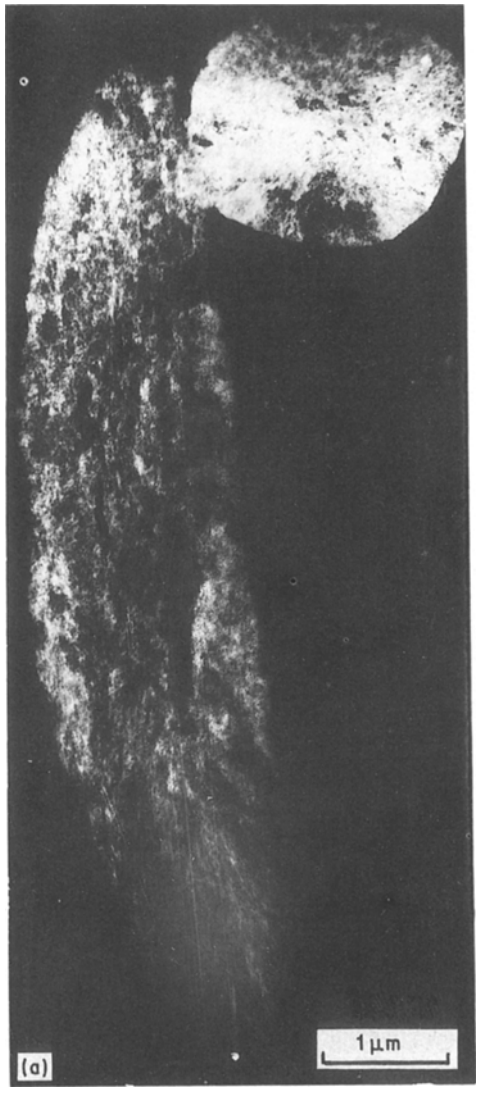

Figure 8 (a) The bright-field image and (b) the SAD pattern of a longitudinal section of the A-type crystal. The bright-field image is rotated through 39° in a clockwise direction with respect to SAD. Note the major axis is parallel to [1 0 0] of θ-$(FeNi)_3B$.

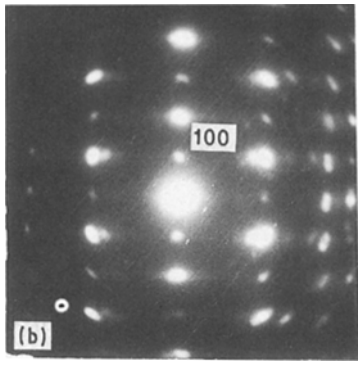

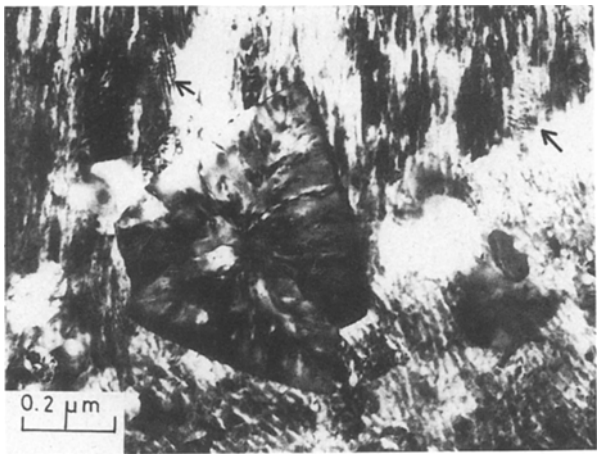

Figure 9 The twinned rods of A-type crystals in the fully crystallized glass (663 K for 150 min).

spherical spot patterns. The SAD patterns yield a lattice constant of 1.07 nm for fcc $(FeNi)_{23}B_6$ and 0.357 nm for γ-FeNi. As the lattice parameter of the former is about three times that of the latter phase, overlap of the SAD patterns occurs. This is in good agreement with an earlier report [9].

As the volume fraction of the B-type crystals is very low, the X-ray diffraction of the annealed samples does not reveal their presence. The thin foil exhibits three types of cross-sectional images, namely, triangular (Fig. 9) hexagonal and square (Fig. 10); of these the triangular is seen in abundance.

The C-type crystals shown in Fig. 4 are spherical in morphology and have γ-FeNi structure as reported earlier [9, 10]. Further examination of the crystallized glass in the scanning electron microscope (SEM) provided useful information regarding the crystallization process. Fig. 11 exemplifies the nature of the first kind of eutectic crystals that could be seen in the SEM. Random orientation of the crystals results in the appearance of different cross-sections varying from rod-like to square crystals. However, an unusual morphology, labelled D, is also seen in the partially crystallized glass (Fig. 12a). Energy dispersive analysis of X-rays (EDAX) at various points of the crystal and the matrix is given in Fig. 12b.

The crystal can be seen to contain two regions. One is a central spherical region and another is its periphery. Spectra 1 and 2 give an approximate composition of iron and nickel at the periphery and at the glassy matrix, respectively. As given by the intensities of the spectra, Fe/Ni ratios remain almost the same for both the glassy matrix and the periphery of the crystal. EDAX analysis performed at the centre of the crystal (spherical region), however, shows (spectrum 3) the Fe/Ni ratio to be higher than that of the matrix and the periphery of the crystal. From these observations it is proposed that the outer region may be a eutectic mixture of γ-FeNi + orthorhombic $(FeNi)_3B$ (because in eutectic crystallization the overall composition of the two phases will be equivalent to that of the matrix). Furthermore, EDAX analysis conducted at the periphery of the crystal shows the intensity of the Fe/Ni ratio to be equivalent to that of the individual γ-FeNi + orthorhombic $(FeNi)_3B$ crystals. Thus the periphery seems to consist of the fast growing A-type crystals. However, due to the rare occurrence of such a combination of crystals and larger size (80 μm), structural analysis by TEM was not possible.

The crystallization kinetics of the A-type crystals which is presumed to affect the stability of the glass due to its very high growth rate has been followed using optical microscopy. A representative optical micrograph of the A-type crystals used for kinetic analysis is shown in Fig. 13. The well-defined dark-contrast particles are crystals formed during annealing. The plots, volume fraction transformed (x) against time (t) and the log length, against the log width of the largest crystal measured for all the isothermal intervals are given in Figs 14 and 15, respectively. Simultaneously, the mean interlamellar spacing for the four isothermal temperatures has also been determined.

4. Discussion

4.1. Kinetics of crystallization

Crystallization of $Fe_{40}Ni_{40}B_{20}$ is complex in the sense that unlike other Fe- and Fe–Ni-base metallic glasses, e.g. $Fe_{80}B_{20}$, $Fe_{50}Ni_{30}B_{20}$ [10] and $Fe_{40}Ni_{40}P_{14}B_6$ [20, 21], four different kinds of crystals nucleate and grow simultaneously. It should be noted that this mode of crystallization is different from the so-called

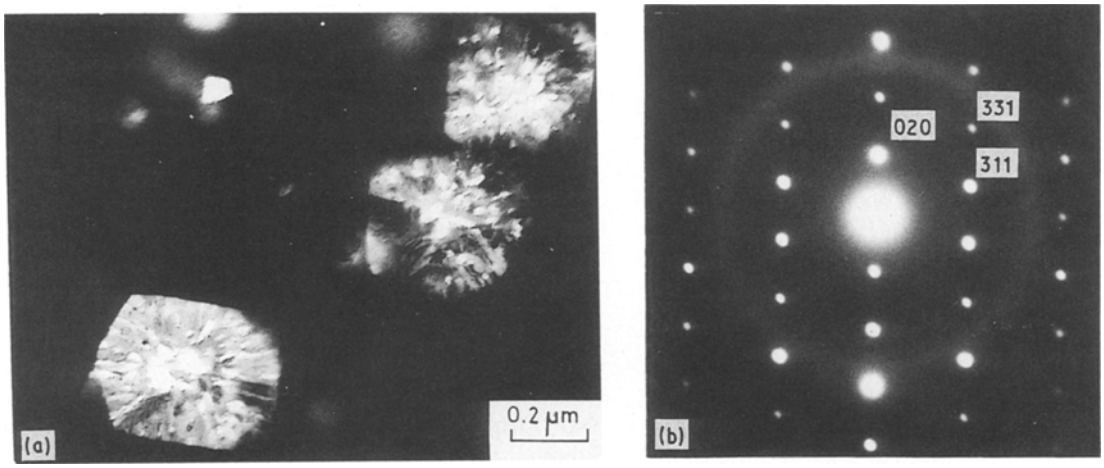

Figure 10 (a) Typical microstructure of the B-type (γ-FeNi + fcc $(FeNi)_{23}B_6$) crystals in the partially crystallized glass (treatment: 663 K for 30 min) and (b) a characteristic SAD pattern obtained from B-type crystals which is indexed for $(FeNi)_{23}B_6$.

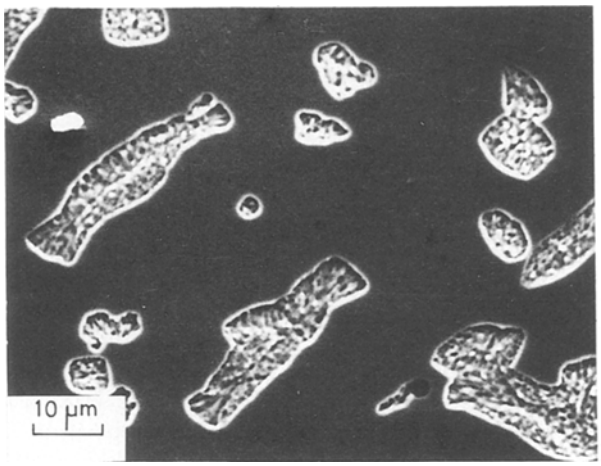

Figure 11 Scanning electron micrograph of a partially crystallized glass showing the fast-growing A-type crystals.

MS I and MS II transformations where the crystallization reactions take place in sequence. This is inferred from the single exothermic peak of the DSC curves (Fig. 1) and the simultaneous occurrence of all the crystals during isothermal annealing of the glass. This result is in agreement with the previous electron microscopic observation [9] and the DSC results [5] while disagreeing with the results of Piller and Haasen [4] who have reported a two-stage crystallizsation into γ-FeNi solid solution followed by a two-phase mixture of γ-FeNi and $(FeNi)_3B$ boride, respectively. From the DSC experiments we have derived $E_c = 323\,kJ\,mol^{-1}$ using the Kissinger method. The value agrees with the first of the two activation energies reported by Piller and Haasen [4], while disagreeing with the low value reported by Luborsky [5]. However, in the present investigation, little significance has been attached to these values, owing to the complexity of the transformation. The prime concern of the investigation is to understand the transformation kinetics of A-type (γ-FeNi + orthorhombic $(FeNi)_3B$) crystals which are presumed to affect the overall thermal stability of the glass. As shown in Fig. 14 the volume fraction (x)–t plots display typical sigmoidal curves characteristic of nucleation and growth processes. These curves can be described by the Johnson–Mehl–Avrami equation

$$X_t = 1 - \exp(-Kt^n)$$

which can be rearranged as

$$\ln[-\ln(1 - x)] = \ln K + n \ln t,$$

where, n and K, respectively, represent the Avrami exponent and a constant.

The Avrami exponent, n, has been obtaned by plotting $\ln - [\ln(1 - x)]$ against $\ln(t - t_0)$ as shown in Fig. 16. The plots do not show any systematic variation for n with temperature while a steady increase in n was reported in 2826 and 2826B glasses [22]. Johnson–Mehl–Avrami analysis gives the idea that the exponent is independent of volume fraction transformed. In a recent article, Calka and Radlinski [23] have shown that this is not so when changes in growth dimensions and competing reactions occur during the progress of transformation. In a Calka plot the first derivative of

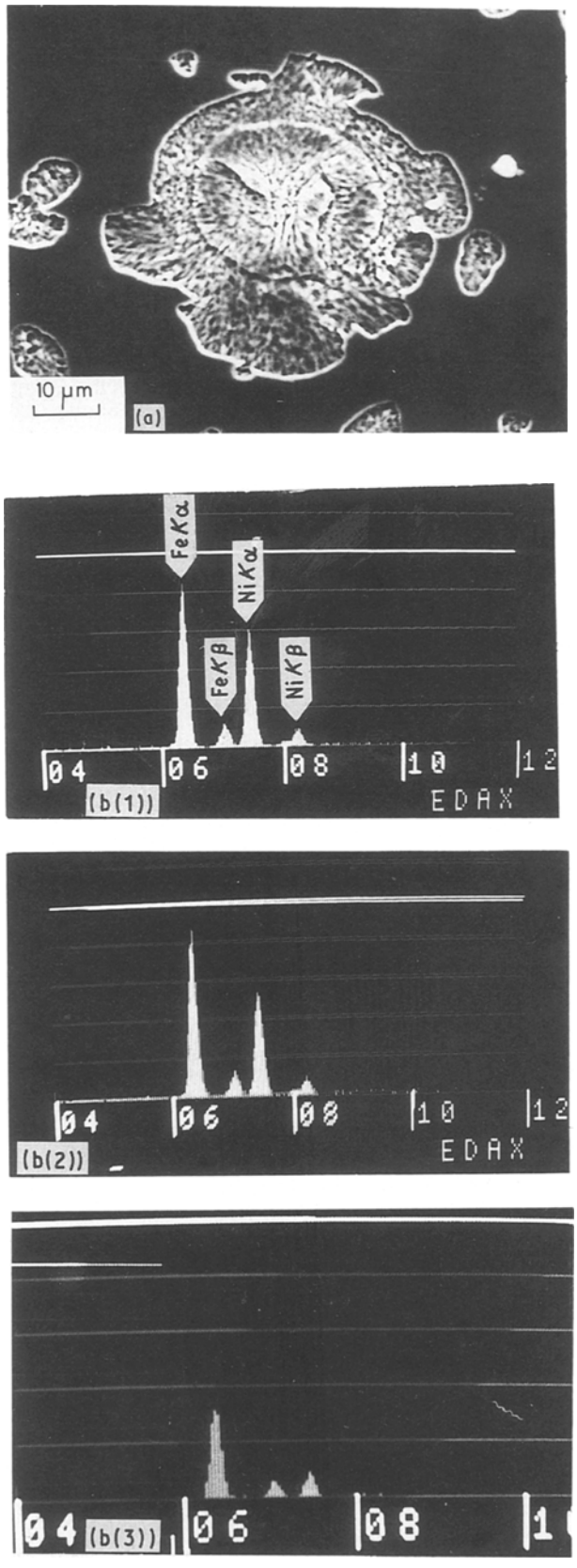

Figure 12 (a) Nucleation of the A-type crystals on an already grown iron-rich spherical crystal of unknown structure (D-type). (b) EDAX spectra of iron and nickel: (1) glassy matrix, (2) periphery of the crystal aggregate and (3) central region of the crystal shown in (a).

Avrami plot is plotted against the volume fraction transformed which tells about the changes in reaction kinetics as the transformation progresses.

Recently, Gibson and Delamore [24] have used Calka analysis for some iron-based metallic glasses

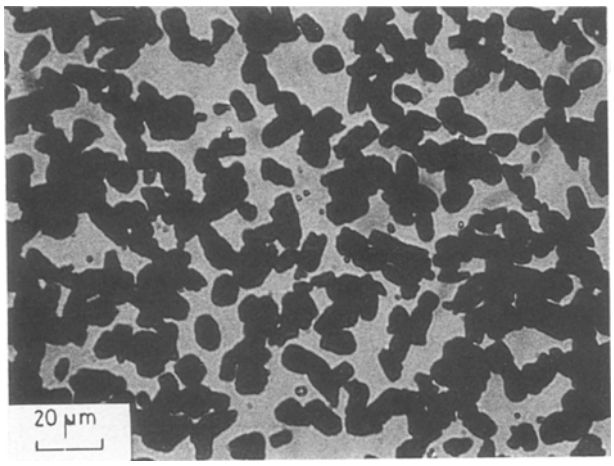

Figure 13 A representative optical micrograph of the annealed glass used to determine the volume fraction of the crystals (annealing conditions 653 K, 2 h).

and found that only in the cases where crystallization took place uniformly within the bulk of the material by a single growth process, was the Avrami exponent independent of temperature and volume fraction transformed.

The plots yield a mean Avrami exponent of 2.08, which is an unusually low value for a eutectic reaction. In a plot of nucleation density, N_v, against time, t, for four isothermal temperatures (628 to 638 K) Muller and Heimendahl (see Fig. 2 in [9]) have noted that N_v does not vary with the time and temperature, characteristic of an athermal nucleation. Consequently, if crystallization is understood to proceed through an athermal nucleation then the Avrami kinetics should yield an exponent of 3.0. However, in assuming a value of 3.0 an isotropic growth of the crystals is presupposed. With any deviation in this to a lower dimensional growth, a lower value for the Avrami exponent is possible. The rod-like morphology of the crystals (Fig. 8) testifies that such a factor should be responsible for the low value of the Avrami exponent. This is also evident from the different growth behaviour of the crystals along the longitudinal and transverse direction of the crystals as seen from Fig. 15. The

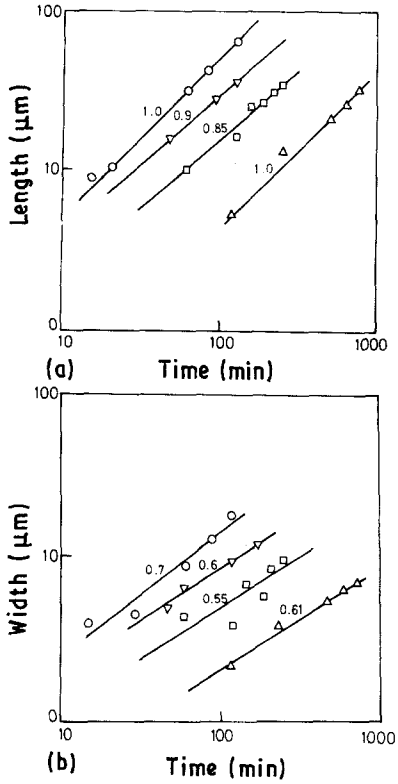

Figure 15 Growth of A-type crystals along (a) major axis and (b) minor axis. (○) 673 K, (▽) 663 K, (□) 653 K, (△) 643 K.

mean slopes of 1.0 and 0.6, respectively, for the longitudinal and radial growths of the crystals leads to the following empirical relations of growth rates.

$$L \propto t^{1.0} \text{ along the longitudinal direction}$$

$$W \propto t^{0.6} \text{ for the transverse direction.}$$

This variation in growth behaviour would result in reducing the value of n to 2.2 which is close to that obtained from the Avrami plots.

One explanation that can be offered to explain the non-linear growth rate along the minor axis is as follows. The fast growing tip (major axis) of the eutectic crystal will reject the excess solute along the sides. So the solute atoms pile up towards the sides of the crystal resulting in a lower growth rate with time along

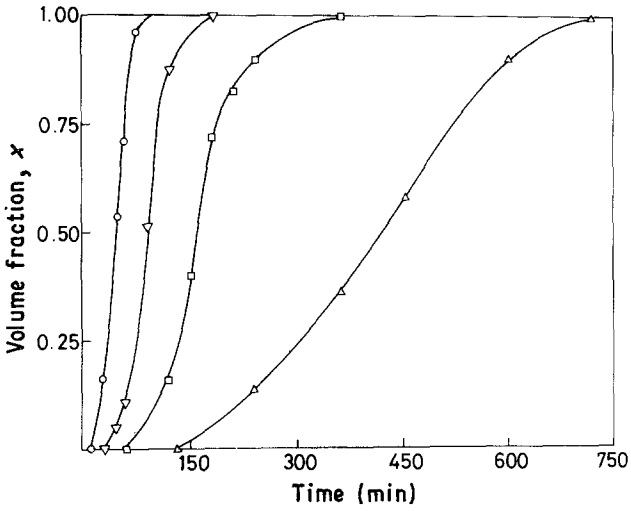

Figure 14 The sigmoidal plots for transformation of A-type crystals. (△) 643 K, (□) 653 K, (▽) 663 K, (○) 673 K.

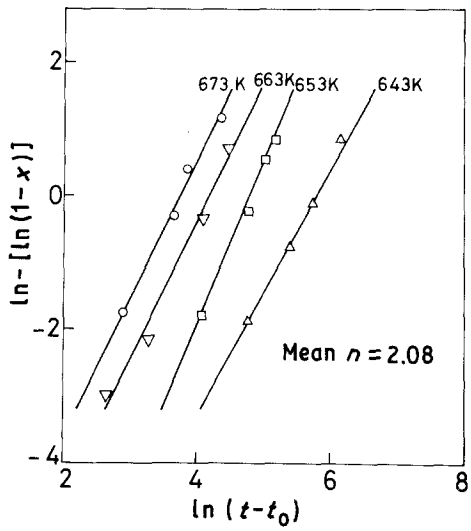

Figure 16 Avrami plots for the A-type crystals.

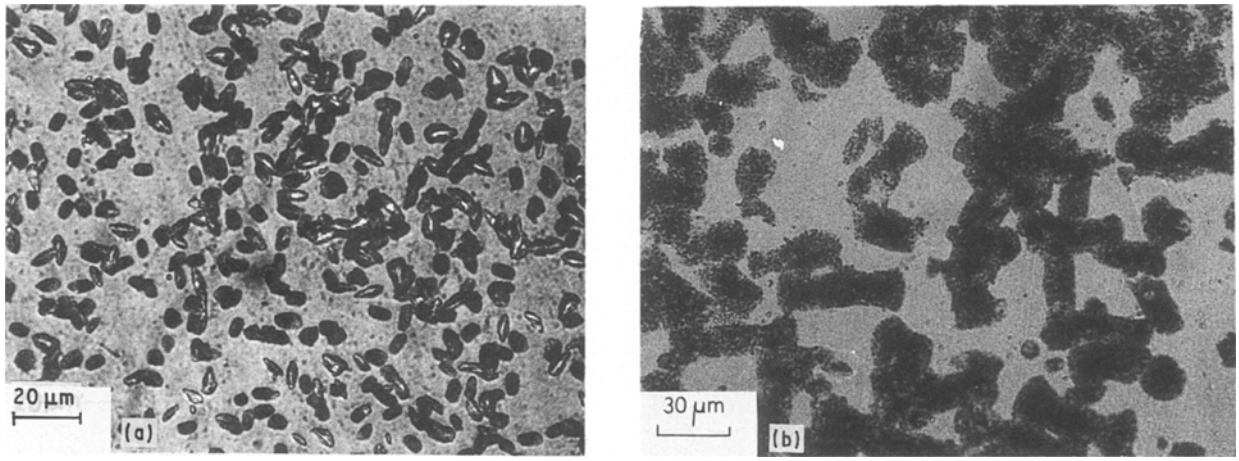

Figure 17 Optical micrographs displaying the difference in aspect ratios in the early and later stages of growth: (a) 673 K, 20 min with aspect ratio 2, and (b) 673 K, 120 min with aspect ratio ≈ 4.

the low growing sides (minor axis) of the crystal. It can be further said that the fast growth along a particular direction during the beginning of the growth may depend on the crystallographic orientation of the phases. These aspects are exemplified by the two optical micrographs showing a lower aspect ratio (≈ 2.0) when just nucleated (Fig. 17a) while exhibiting a larger aspect ratio (≈ 4.0) in the almost fully crystallized condition (Fig. 17b).

The activation energy for crystallization has been calculated from the time taken for 50% crystallization ($t_{0.5}$) using Fig. 14 which turns out to be 237 kJ mol^{-1}. The value is lower than those determined from DSC results of the present investigation (323 kJ mol^{-1}) and the DSC and coercivity results of Luborsky [5] (280 kJ mol^{-1}). However, determination of the activation energy from DSC and coercivity cannot be achieved for a particular crystallization process of interest where more than one reaction proceeds in a parallel manner.

In order to determine the apparent diffusivity, a mean value of interlamellar spacing, λ, was obtained by measuring over 100 interlamellar spacings at each temperature. Interestingly, the values were found to increase with decreasing temperature in agreement with Tiwari *et al.* [21]. Using the relation $D^{app} = U\lambda^{min}/4$, diffusivity has been calculated for various temperatures and plotted as shown in Fig. 18. In the same figure the diffusivity values obtained by Cahn *et al.* [12] using secondary ion mass spectroscopy (SIMS) for the diffusion of boron for the same alloy, and diffusivity values of Tiwari *et al.* [21] for $Fe_{40}Ni_{40}P_{16}B_4$ glass deduced from the lamellar spacing, are plotted for comparison. Apparently, the diffusivity values lie in the same range as that of Cahn *et al.* [12] indicating that the diffusivity corresponds to boron diffusion. However, a closer examination shows that the diffusion coefficients obtained by Cahn *et al.* increase quickly with temperature, while the present results show only a marginal increase of D with temperature. The reason for this discrepancy is not clear.

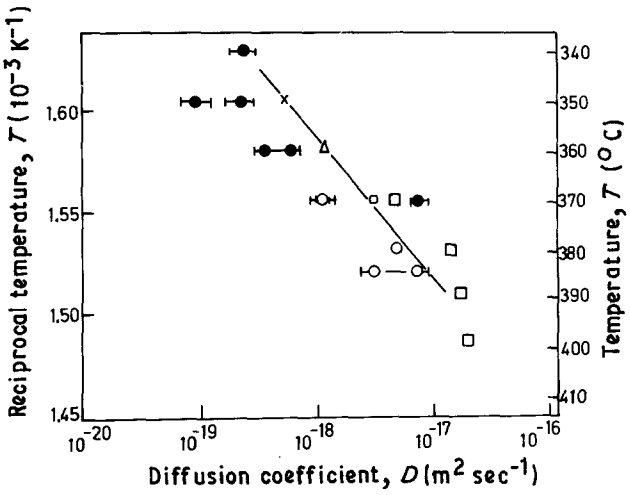

Figure 18 Comparison of the diffusion coefficients in $Fe_{40}Ni_{40}B_{20}$ and $Fe_{40}Ni_{40}P_{16}B_4$. The diffusion coefficients of $Fe_{40}Ni_{40}P_{16}B_4$ are joined by a linear curve. (●) Amorphous and (○) partially crystalline samples [12]. (×, △, □, ○) [21], (□) present work.

4.2. Phase relationships

The Vitrovac 0040 glass crystallizes into four phases, namely γ-FeNi, orthorhombic $(FeNi)_3B$, fcc $(FeNi)_{23}B_6$ and an unknown phase rich in iron content and low in nickel content, in the range 643 to 673 K. The combination of γ-FeNi with these two borides results in two kinds of eutectic crystals and its independent crystallization leads to a primary reaction. This is in accordance with Muller and Heimendahl [9]. On the contrary, Duhaj and Svec [10] reported bct $(FeNi)_3B$ phase instead of fcc $(FeNi)_{23}B_6$ phase. Fig. 10b makes it clear that the interplanar distance of

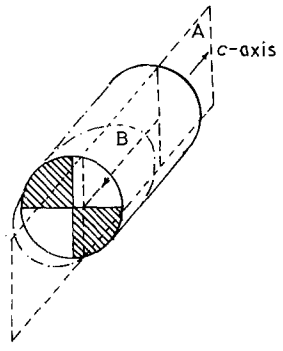

Figure 19 Schematic drawing to illustrate various cross-sectional images of the crystals [20].

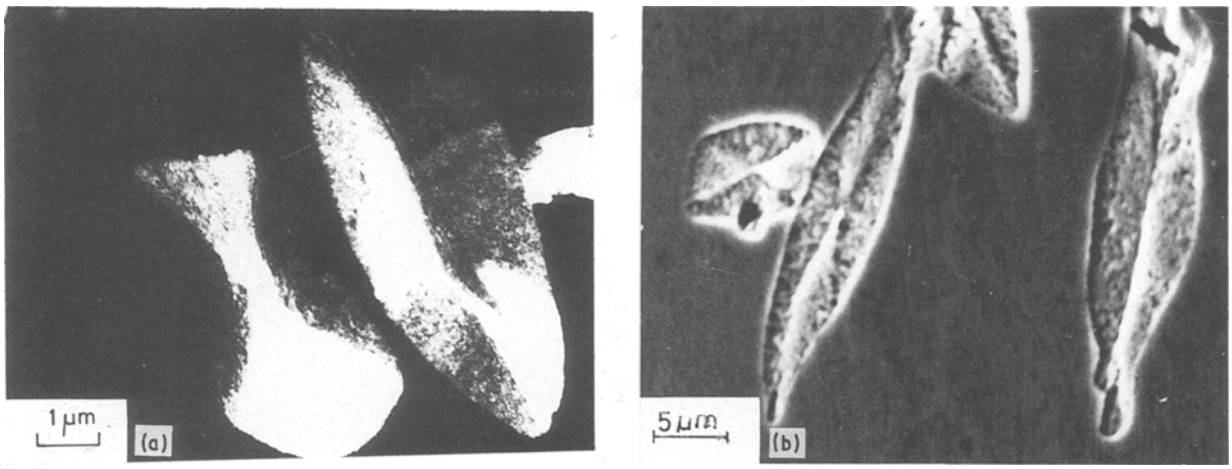

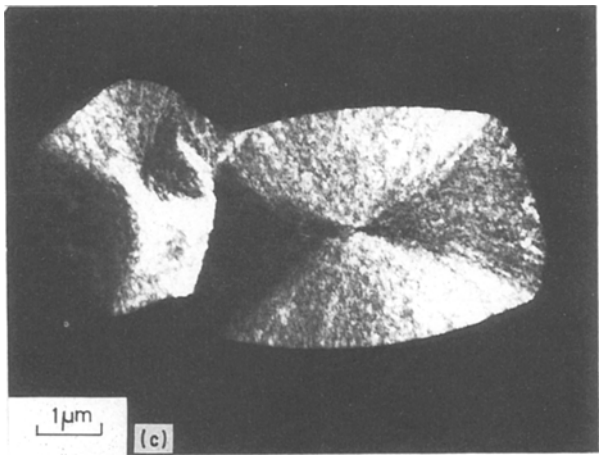

Figure 20 Bisection of the crystal along the mid-rib, showing different contrast in (a) TEM and (b) SEM. A different cross-section other than this shows four quadrants (c).

0.532 nm in the SAD pattern cannot be indexed for any possible planes of bct $(FeNi)_3B$ phase with the lattice parameters of $a = 0.862$ nm and $c = 0.492$ nm but for the (0 2 0) of fcc $(FeNi)_{23}B_6$ phase with the lattice constant $a = 1.07$ nm. The occurrence of such a cubic boride phase is common in Fe–B–C [25] and Fe–Ni–Mo–B [26] glasses. Another point which lends support is that, if these eutectic crystals were to be γ-FeNi + bct $(FeNi)_3B$, then there must be some resemblance in growth morphology and growth rates with that of γ-FeNi + bct $(FeNi)_3B$ found in $Fe_{50}Ni_{30}B_{20}$ [19] and $Fe_{40}Ni_{40}P_{16}B_4$ [20, 21] glasses which have not been observed.

While it is not possible to explain the simultaneous formation of three types of crystal on the basis of a simple ternary diagram, it could be possible to visualize the formation of these crystals from the glass which probably has undergone phase separation into two glasses (G_1 and G_2). While the first glass (G_1) crystallizes directly into A-type crystals (γ-FeNi + θ–$\gamma(FeNi)_3B$) the second glass may further decompose into primary crystals of γ-FeNi and G_3 which subsequently transforms into γ-FeNi + fcc $(FeNi)_{23}B_6$ crystals by a eutectic mode. It is noteworthy that Piller and Haasen [4] detected phase separation of the glass, though the present study could not confirm this. The formation of the γ-FeNi and orthorhombic $(FeNi)_3B$ phase in this high nickel-containing glass is in conformity with Battezzati *et al.* [26]. However, as indicated by Stubicar *et al.* [6], the orthorhombic $(FeNi)_3B$ transforms to γ-FeNi above 1023 K.

4.3. Morphology of transformation products

The four types of crystal formed during annealing of $Fe_{40}Ni_{40}B_{20}$ glass differ in morphology to varying degrees. The fast growing eutectic (A) has a cylindrical morphology while the second eutectic (B) with a slower growth rate has a cuboidal morphology. The third crystal (C) with a single phase and the fourth crystal (D) of unknown phase have spherical morphologies.

Various images of the A crystals observed under TEM can be explained due to several sections the foil could make on the cylindrical crystals – a schematic explanation by Walter *et al.* [19] in the case of the crystals formed in $Fe_{80}B_{20}$ and $Fe_{50}Ni_{30}B_{20}$ glasses as indicated in Fig. 19 could well be used to explain the different cross-sections noticed under TEM. The hatched quadrants of the cross-section represent one set of twins, while the unhatched quadrants belong to another set of twins. If the plane of the foil intersects in a longitudinal direction, i.e. parallel to the c-axis as shown in the figure as section A, but not in the mid-plane, it would show two orientations roughly separated by a line drawn through the middle of the section parallel to the c-axis. Such a resultant morphology is exemplified using transmission and scanning electron micrographs (Fig. 20a, b). Any section other than this would show four quadrants (Fig. 20c). The difference in orientation of the phases in the two halves of the crystals is brought out in Fig. 21. The dark-field image corresponding to the spot marked in SAD illuminates only one-half of the bright-field image, clearly testifying to the difference in orientation relation between the two halves of the crystals.

A close observation of the microstructure (Fig. 9) and the electron diffraction pattern (Fig. 8b) suggests the existence of twins in the orthorhombic phase in agreement with Walter *et al.* [19] who found twinning of the bct phase in γ-FeNi + bct $(FeNi)_3B$ eutectic crystals, while twin formation has been ascribed to accommodate strain due to density differences between the amorphous and crystalline phases following devitrification [27]. Interestingly, a similar observation has been made during cellular

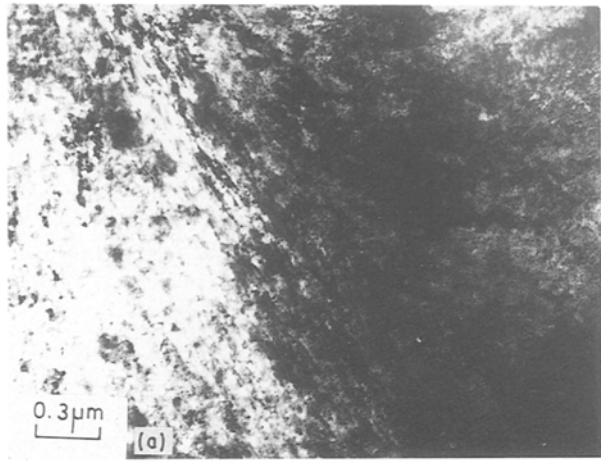

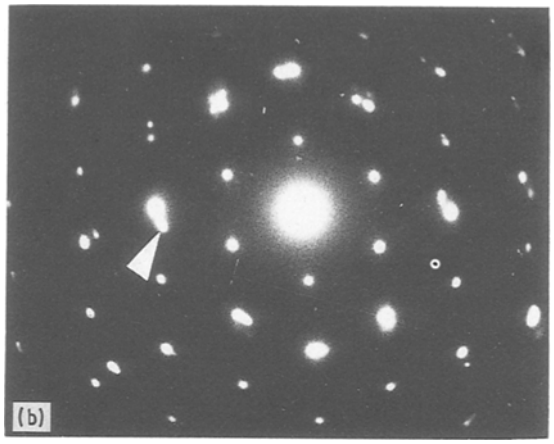

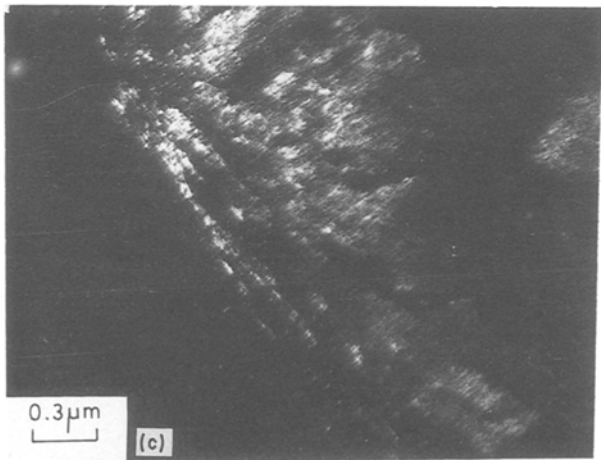

Figure 21 The differing orientations of the phases along the mid-rib of the crystal. (a) Bright field, (b) SAD pattern indicating twins, and (c) dark-field image corresponding to the spot marked by an arrow in the SAD. Note only one-half of the crystal is illuminated.

transformation in crystalline alloys as well, which according to Ecob and Ralph [28] is due to the higher growth rates of the phase and the lower diffusivity of the solute. This argument is further supported by the fact that such twins do not exist in the B-type eutectic crystal whose growth rate has been found to be about 47 times lower than that of the A-type eutectic crystal.

The observation of different images (triangular, square and hexagonal) of B-type crystals can be attributed to its cuboidal morphology. Although Muller and Heimendahl [9] have proposed the existence of several morphologies for this crystal, they have not given sufficient evidence. Unlike A-type crystals, B-type crystals do not show four quadrants having differing orientation. On the contrary, the SAD patterns show well-defined spots indicating the same kind of orientation throughout the section of the crystal (Fig. 10b).

Although the A- and B-type crystals grow by the same eutectic mechanism, their morphologies and growth rates differ considerably. It may be possible that both $(FeNi)_3B$ and $(FeNi)_{23}B_6$ phases nucleate during the early stages of crystallization which aids the formation of γ-FeNi phase resulting in eutectic crystals. The formation of $(FeNi)_3B$ phase in preference to γ-FeNi has also been proposed by Muller and Heimendahl [9]. Thus the growth behaviour and the morphology of the eutectic precipitates depend on the growth characteristics of both the boride phases. In this regard, it is interesting to note that the growth rate of A-type eutectic crystals is comparable to γ-Fe + bct Fe_3B eutectic crystals in $Fe_{80}B_{20}$ glass [29] and γ-FeNi + bct $(FeNi)_3B$ eutectic crystals in $Fe_{40}Ni_{40}P_{16}B_4$ glass [21]. The alloying elements also seem to affect the morphology, as ellipsoidal, cylindrical and cuboidal crystals can be found, respectively, in $Fe_{80}B_{20}$, $Fe_{40}Ni_{40}B_{20}$ and $Fe_{40}Ni_{40}P_{16}B_4$ glasses.

The TEM image of γ-FeNi phases having different radii indicates that the crystals have spherical morphology. The spherical morphology of γ-FeNi phases is consistent with other glasses like $Fe_{32}Ni_{36}Cr_{14}B_{12}B_6$ where the glass undergoes primary crystallization [30].

The SEM image of the iron-rich D-type crystals show a circular cross-section indicating that these crystals must also be spherical in morphology. The interesting behaviour of these crystals is that they aid the nucleation of A-type eutectic crystals. This is understandable, because eutectic crystallization normally requires higher activation energy for nucleation compared to that of either primary or polymorphic reactions [31]. The iron-rich Fe–Ni solid solution normally occurs (by primary crystallization) in metal-rich metal–metalloid glasses. However, it should be mentioned that Heimendahl [32] has detected an iron-rich solid solution in $Fe_{32}Ni_{36}Cr_{14}P_{12}B_6$ glass using high-resolution microscopy, which was not reported earlier. The size of these crystals, however, is comparatively smaller than the size of the crystals which are reported here.

5. Conclusions

1. Vitrovac 0040 crystallizes simultaneously into four types of crystal: (A) γ-FeNi + θ-$(FeNi)_3B$, (B) γ-FeNi + fcc $(FeNi)_{23}B_6$, (C) γ-FeNi solid solution, and (D) an unknown iron-rich phase.

2. The study of transformation kinetics of A-type crystals yields the activation energy 237 kJ mol^{-1} for crystallization. The low value of 2.08 for the Avrami exponent has been interpreted due to athermal nucleation and anisotropic growth of the crystals.

3. The A-type crystals have a rod-like morphology with an aspect ratio of ≈ 4 in the fully crystallized

condition. The orthorhombic phase of this crystal displays twinning.

4. It is inferred that Vitrovac 0040 undergoes phase separation into two glasses, G_1 and G_2, prior to crystallization. While G_1 can give rise to A-type eutectic crystals directly, G_2 can transform to primary γ-FeNi crystals and G_3. The latter subsequently crystallizes into B-type crystals by the eutectic mode.

Acknowledgements

The authors thank the Department of Science and Technology, Government of India for financial assistance and Mr B. S. Murty for useful discussions.

References

1. M. G. SCOTT and A. KURSUMOVIC, *Acta Metall.* **30** (1982) 853.
2. A. VAN DEN BEUKEL, S. VAN DER ZWAAZ and A. L. MULDER, *ibid.* **32** (1984) 1985.
3. A. VAN DEN BEUKEL *et al.*, *ibid.* **34** (1986) 482.
4. J. PILLER and P. HAASEN, *ibid.* **30** (1982) 1.
5. F. E. LUBORSKY, *Mat. Sci. Engng* **28** (1977) 138.
6. M. STUBICAR *et al.*, *Phys. Status Solidi* (*a*) **44** (1977) 339.
7. B. STEFFEN and G. LIEDTKE, *Z. Metallkde* **72** (1981) 849.
8. V. S. RAJA, KISHORE and S. RANGANATHAN, in "Rapidly Quenched Metals V", Vol. II, edited by S. Steeb and H. Warlimont (Elsevier, Amsterdam, 1985) p. 1485.
9. K. MULLER and M. V. HEIMENDAHL, *J. Mater. Sci.* **17** (1982) 2525.
10. P. DUHAJ and P. SVEC, *Phys. Status Solidi* (*a*) **80** (1983) 231.
11. J. CERMAK *et al.*, *ibid.* **91** (1985) 407.
12. R. W. CAHN *et al.*, *J. Mater. Sci.* **15** (1980) 702.
13. G. C. CHI, H. S. CHEN and C. E. MILLER, *J. Appl. Phys.* **49** (1978) 1715.
14. S. TAKAYAMA and T. OI, *ibid.* **50** (1979) 1595.
15. U. KOSTER, U. HEROLD and H. G. HILLENBRAND, *Scripta Metall.* **17** (1983) 867.
16. V. S. RAJA, KISHORE and S. RANGANATHAN, *Bull. Mater. Sci.* **9** (1987) 207.
17. G. F. VANDER VOORT, "Metallography Principles and Practice" (McGraw Hill, New York, 1984) p. 426.
18. H. E. KISSINGER, *Anal. Chem.* **29** (1957) 1702.
19. J. L. WALTER, S. F. BARTRAM and R. R. RUSSELL, *Met. Trans.* **9A** (1978) 803.
20. J. L. WALTER *et al.*, *ibid.* **8A** (1977) 1141.
21. R. S. TIWARI, S. RANGANATHAN and M. V. HEIMENDAHL, *Z. Metallkde* **72** (1981) 563.
22. M. G. SCOTT, *J. Mater. Sci.* **13** (1978) 291.
23. A. CALKA and A. P. RADLINSKI, in "Proceedings of Fall Meeting 1986" (Materials Research Society, Boston, Massachusetts).
24. M. A. GIBSON and G. W. DELAMORE, *J. Mater. Sci.* **22** (1987) 4550.
25. U. HEROLD and U. KOSTER, *Z. Metallkde* **69** (1978) 326.
26. L. BATTEZZATI, C. ANTONIONE and A. COSSOLO, *ibid.* **73** (1982) 185.
27. U. KOSTER, in "Phase Transformations in Crystalline and Amorphous Alloys", edited by B. L. Mordike (Deutsche Gesellschaft fuer Metallkunde, Germany, 1983) p. 113.
28. E. C. ECOB and B. RALPH, in "Solid–Solid Phase Transformations", edited by H. I. Aaronson, D. E. Laughlin, R. F. Sekerka and C. M. Wayman (AIME, Warrendale, 1981) p. 939.
29. A. L. GREER, *Acta Metall.* **30** (1982) 171.
30. M. V. HEIMENDAHL and G. KUGLSTATTER, *J. Mater. Sci.* **16** (1981) 2405.
31. S. RANGANATHAN, J. C. CLAUS, R. S. TIWARI and M. V. HEIMENDAHL, in Proceedings of the Conference on Metallic Glasses, Budapest, 1980. (Science and Technology, Budapest, 1980).
32. M. V. HEIMENDAHL, *Mater. Sci. Engng* **68** (1985) 43.

Received 1 June
and accepted 23 October 1989